*Nano Research* 2015, 8(10): 3237–3249
DOI 10.1007/s12274-015-0824-9
**Research Article**
ISSN 1998-0124
CN 11-5974/O4

# M@MIL-100(Fe) (M = Au, Pd, Pt) nanocomposites fabricated by a facile photodeposition process: Efficient visible-light photocatalysts for redox reactions in water

Ruowen Liang, Fenfen Jing, Lijuan Shen, Na Qin, and Ling Wu (✉)

*State Key Laboratory of Photocatalysis on Energy and Environment, Fuzhou University, Fuzhou 350002, China*

**Received:** 10 April 2015
**Revised:** 13 May 2015
**Accepted:** 25 May 2015



**KEYWORDS**
MIL-100(Fe),
photodeposition,
noble metal,
redox reactions

## ABSTRACT

Proper design and preparation of high-performance and stable dual functional photocatalytic materials remains a significant objective of research. In this work, highly dispersed noble-metal nanoparticles (Au, Pd, Pt) were immobilized on MIL-100(Fe) (denoted M@MIL-100(Fe)) using a facile room-temperature photodeposition technique. The resulting M@MIL-100(Fe) (M = Au, Pd, and Pt) nanocomposites exhibited enhanced photoactivities toward photocatalytic degradation of methyl orange (MO) and reduction of heavy-metal Cr(VI) ions under visible-light irradiation ($\lambda \geqslant 420$ nm) compared with blank-MIL-100(Fe). Combining these results with photoelectrochemical analyses revealed that noble-metal deposition can effectively improve the charge-separation efficiency of MIL-100(Fe) under visible-light irradiation. This phenomenon in turn leads to the enhancement of visible-light-driven photoactivity of M@MIL-100(Fe) toward photocatalytic redox reactions. In particular, the Pt@MIL-100(Fe) with an average Pt particle size of 2 nm exhibited remarkably enhanced photoactivities compared with those of M@MIL-100(Fe) (M = Au and Pd), which can be attributed to the integrative effect of the enhanced light absorption intensity and more efficient separation of the photogenerated charge carrier. In addition, possible photocatalytic reaction mechanisms are also proposed.

## 1 Introduction

Metal-organic frameworks (MOFs) are a new class of hybrid porous materials that possess 3D crystalline frameworks composed of metal-oxo clusters and organic linkers [1–3]. Because of their inherent structural characteristics, such as large surface areas and well-ordered porous structures, these materials are used as gas adsorbents, catalyst supports, and catalysts as well as agents for separation and drug delivery [4–9]. Currently, a new burgeoning direction in the field of MOFs is their use as photocatalysts [10–12]. Since the first report of photocatalytic activity in MOF-5, MOFs have been increasingly used as novel photocatalysts

Address correspondence to wuling@fzu.edu.cn

[13, 14]. However, they still suffer from some drawbacks, such as a high recombination probability of photoexcited charge carriers. To improve their photocatalytic performances, some researchers have focused their efforts on the introduction of functional entities (e.g., metal complexes, metal salts, or metal and metal oxide particles) into MOF materials [15, 16].

It is commonly accepted that improving the utilization efficiency of photogenerated electron–hole pairs and prolonging the lifetime of photogenerated charge carriers are expected to enhance the photoactivity toward target reactions. In this regard, noble-metal nanoparticles (NPs) could be a promising selection for photocatalyst promoters. The high Fermi energy level of noble-metal NPs can efficiently separate photoexcited electron–hole pairs of the photocatalyst, which could improve the photoactivity toward target reactions [17–20]. It has been previously demonstrated that MOFs are particularly promising as supports for noble-metal NP immobilization because of their ultrahigh surface area and moderate thermal stability, which are important for controlling the limited growth of metal NPs and producing highly reactive monodispersed metal NPs [21]. Therefore, the integration of noble-metal NPs with MOF photocatalysts in an appropriate manner would further improve the photocatalytic activity of MOFs. To date, various methods, including chemical vapor deposition, colloidal synthesis, and incipient wetness impregnation, have been developed to fabricate noble-metal@MOF nanocomposites (denoted as M@MOFs) [22–26]. However, these routes typically result in high energy consumption, large agglomerated particles with irregular morphologies, and insufficient interfacial contact between the supports and noble-metal NPs. Sometimes, the reducing agents, typically $NaBH_4$, can destroy the supports. Because of these problems, synthesizing high-performance M@MOF photocatalysts without using reducing agents or organic stabilizers remains a challenge. Although there are some reports on metal@semiconductor photocatalysts [17, 20], reports on the photocatalytic performance of M@MOFs are rather scarce. In particular, the relations with different noble metals and the particle size of metal NPs have not been studied thus far.

As a typical MOF material, MIL-100(Fe) is of special interest because of its high chemical stability and water stability. In addition, considering its photoactive property, MIL-100(Fe) is a promising candidate for the development of efficient photocatalysts [14, 27]. Toward this end, we report on a set of noble-metal@MIL-100(Fe) (M = Au, Pd, Pt) nanocomposites (denoted M@MIL-100(Fe)) fabricated using a facile room-temperature photodeposition technique without the use of any chemical reducing agents or organic stabilizers. Once MIL-100(Fe) is dispersed in absolute ethanol and irradiated by visible light ($\lambda \geqslant 420$ nm), the photogenerated holes are scavenged by ethanol, whereas the photogenerated electrons are trapped by metal ions, and M@MIL-100(Fe) with intimate interfacial contact are obtained. The as-synthesized M@MIL-100(Fe) nanocomposites exhibited remarkably enhanced visible-light photoactivity toward the oxidation of dye and reduction of Cr(VI) under visible-light irradiation ($\lambda \geqslant 420$ nm). The origin of the improved photoactivity and the underlying reaction mechanism were studied in a series of characterization and trapping experiments. In particular, the Pt@MIL-100(Fe) with an average Pt particle size of 2 nm exhibited remarkably enhanced activities for photocatalytic redox reactions compared with MIL-100(Fe), Au@MIL-100(Fe), and Pd@MIL-100(Fe). This enhancement can be attributed to the integrative effect of the enhanced light absorption intensity and more efficient separation of the photogenerated charge carriers. In addition, photocatalytic mechanisms for the dye oxidation and reduction of Cr(VI) over M@MIL-100(Fe) are also proposed.

## 2 Experimental

### 2.1 Reagents and chemicals

All the chemicals were obtained from commercial sources and used without further purification. Palladium chloride ($PdCl_2$), hydrochloric acid (HCl, 37%), hydrofluoric acid (HF, 49%), nitric acid ($HNO_3$, 68%), hydrogen peroxide ($H_2O_2$, 30%), hydrogen tetrachloroaurate (III) tetrahydrate ($HAuCl_4{\cdot}4H_2O$), hexachloroplatinic (IV) acid hexahydrate ($H_2PtCl_6{\cdot}6H_2O$), palladium (II) chloride ($PdCl_2$), and anhydrous ethanol were purchased from Sinopharm Chemical Reagent Co. Ltd., China. Iron powder (99%) was supplied

by Aladdin Reagent Co., Ltd. (Shanghai, China). Benzene-1,3,5-tricarboxylic acid ($H_3BTC$, 99%) was supplied by Alfa Aesar China Co., Ltd. (Tianjin, China).

### 2.2 Synthesis of MIL-100(Fe)

MIL-100(Fe) was synthesized according to the method previously reported by Férey et al. [27]. Iron powder (277.5 mg), $H_3BTC$ (687.5 mg), HF (48%, 200 μL), and $HNO_3$ (65%, 190 μL) were well mixed with 20 mL of deionized water in a Teflon liner. After stirring at 500 rpm for 30 min, the Teflon liner was sealed in a stainless steel bomb and heated at 150 ℃ for 24 h. After the heat treatment, the autoclave was allowed to cool naturally to room temperature, and the product was collected by centrifugation at 4,000 rpm for 5 min. A treatment in hot water (60 ℃) for 3 h was applied to remove the residual $H_3BTC$. Then, the obtained saffron yellow powder was centrifuged at 4,000 rpm for 5 min and dried under vacuum at 100 ℃ for 12 h.

### 2.3 Fabrication of M@MIL-100(Fe) (M = Au, Pd, Pt) nanocomposites

The precursors of Au and Pt were directly dissolved in deionized water to produce a corresponding solution with a desirable concentration, 10 mg/mL. Because $PdCl_2$ is slightly soluble in water, HCl was used to dissolve it. The resulting $H_2PdCl_4$ solution had the same concentration of 10 mg/mL as that of the precursor solution of Au or Pt. In a typical experiment, a mixture of MIL-100(Fe) (100 mg), a given amount of metal-ion aqueous solution (0.210 mL of $HAuCl_4$, 0.265 mL of $H_2PtCl_6$, or 0.345 mL of $H_2PdCl_4$), and ethanol (5 mL) were added to 10 mL of $H_2O$ in a quartz vial. Before the irradiation process, gaseous $N_2$ was bubbled through the solution to ensure that the solution did not contain dissolved $O_2$. Then, the suspension was irradiated for 60 min under visible light ($\lambda \geqslant 420$ nm). After that, the obtained samples were washed with ethanol several times and blow-dried with $N_2$. The obtained samples were labeled as Au@MIL-100(Fe), Pd@MIL-100(Fe), and Pt@MIL-100(Fe).

### 2.4 Characterization

X-ray diffraction (XRD) patterns were obtained using a Bruker D8 Advance X-ray diffractometer operated at 40 kV and 40 mA with Ni-filtered Cu K$\alpha$ irradiation ($\lambda$ = 0.15406 nm). The data were recorded in the 2$\theta$ range of 3°–60°. Transmission electron microscopy (TEM) and high-resolution TEM (HRTEM) images were obtained using a JEOL model JEM2010 EX microscope at an accelerating voltage of 200 kV. X-ray photoelectron spectroscopy (XPS) measurements were conducted on a PHI Quantum 2000 XPS system equipped with an Al X-ray source (1,486.6 eV). The Brunauer–Emmett–Teller (BET) surface area was measured using an ASAP2020M apparatus (Micromeritics Instrument Corp., USA). UV-vis diffuse reflectance spectra (DRS) were recorded on a Cary-500 UV-vis-NIR spectrometer in which $BaSO_4$ powder was used as the internal standard. Inductively coupled plasma optical emission spectroscopy (ICP) measurements were performed using an Ultima2 ICP optical emission spectrometer. The mineralization degree of the dye aqueous solutions was detected based on the total organic carbon (TOC) value, which was obtained using a Shimadzu TOC-VCPH analyzer. Mott–Schottky analysis was performed at a Zahner electrochemical workstation. The photocurrent measurements were conducted on a Precision PARC workstation. Photoluminescence (PL) spectra of the samples were obtained on an Edinburgh FL/FS900 spectrophotometer.

### 2.5 Evaluation of photocatalytic activity

The photocatalytic degradation of methyl orange (MO) was performed at 30 ℃ in a 100-mL quartz reactor containing 5 mg photocatalyst and 40 mL of a 20 mg/L MO aqueous solution. The pH value (pH 4) of the reaction solution was adjusted using 2 M $H_2SO_4$. After adding 40 μL of $H_2O_2$, the suspension was stirred in the dark for 50 min to ensure the establishment of adsorption–desorption equilibrium, and the suspension was irradiated by a 300-W Xe lamp (PLS-SXE 300, Trusttech Co. Ltd., Beijing) with a 420-nm cut-off filter (420 nm $\leqslant \lambda \leqslant$ 760 nm). As the reaction proceeded, approximately 3 mL of the suspension was collected from the reactor at a scheduled interval and centrifuged to separate the photocatalyst. The filtrate was analyzed by recording variations of the maximum absorption band ($\lambda$ = 464 nm) in the UV-vis spectra of MO using a Cary 50 UV-vis spectrophotometer (Varian Co.). For the

photocatalytic reduction of heavy Cr(VI) ions in water, the photocatalyst (40 mg) and ammonium oxalate (5 mg) were dispersed in 40 mL of Cr(VI) aqueous solution (20 mg/L, pH 4) in a quartz reactor. The rest of the procedure for the resulting suspension was the same as that of the photocatalytic degradation of MO except that the Cr(VI) content was determined at 540 nm using the diphenylcarbazide method (DPC) with a Cary 50 UV-vis spectrophotometer (Varian Co.) [28].

## 3 Results and discussion

### 3.1 Characterization

Noble-metal (Au, Pd, and Pt) NPs deposited on MIL-100(Fe), denoted as M@MIL-100(Fe), were prepared via a facile room-temperature photodeposition method, as illustrated in Scheme 1. Once MIL-100(Fe) was dispersed in absolute ethanol and subsequently irradiated by visible light ($\lambda \geqslant 420$ nm), the photogenerated holes were scavenged by ethanol, whereas the photogenerated electrons were trapped by metal ions. Then, M@MIL-100(Fe) nanocomposites with intimate interfacial contact were obtained. The XRD patterns of the as-prepared MIL-100(Fe) and M@MIL-100(Fe) (M = Au, Pd, and Pt) are presented in Fig. 1. It is apparent that the M@MIL-100(Fe) nanocomposites with different metal loadings exhibit similar XRD patterns, suggesting that the integrity of the MIL-100(Fe) framework is maintained. Moreover, no characteristic diffractions for Au, Pd, and Pt are observed in the M@MIL-100(Fe). This result may be due to the high distribution and low weight loading of metal NPs on the surface of MIL-100(Fe) (1 wt.%).

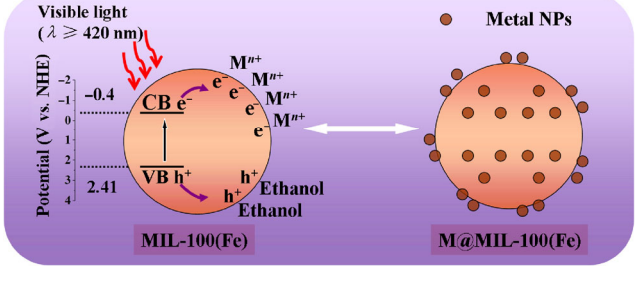


**Scheme 1** Photodeposition route for formation of M@MIL-100(Fe) nanocomposites. CB: conduction band; VB: valence band; M: Au, Pd, Pt; $e^-$: photoexcited electrons; $h^+$: photoexcited holes; NPs: nanoparticles.

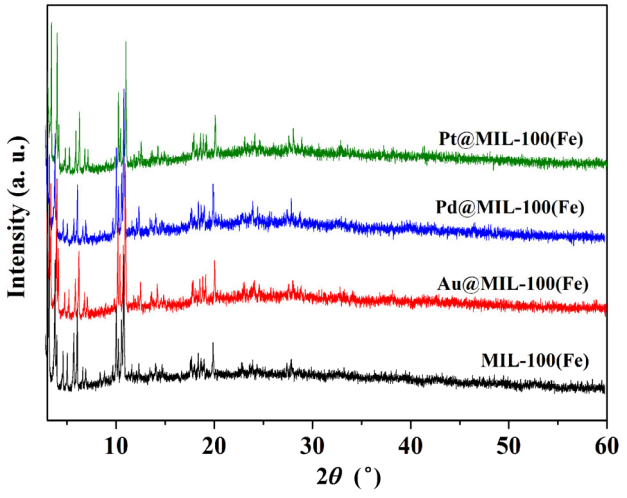


**Figure 1** XRD patterns of MIL-100(Fe) and M@MIL-100(Fe) (M = Au, Pd, and Pt).

To ascertain the details of the surface chemical states of the samples, XPS measurements were performed. Figure 2(a) presents overall surveys of the as-synthesized M@MIL-100(Fe) (M = Au, Pd, and Pt) nanocomposites, which clearly reveal C, O, Fe, and noble-metal element signals. Well-defined peaks corresponding to metallic Au, Pd, and Pt species can also be detected (Figs. 2(b)–2(d)). Figure 2(b) shows the binding energies of Au $4f_{7/2}$ and Au $4f_{5/2}$, which are located at approximately 82.9 and 87.5 eV, respectively, indicating that the oxidation states of Au on MIL-100(Fe) are metallic $Au^0$ [29, 30]. Similarly, the doublet with binding energies of 335.5 (Pd $3d_{5/2}$) and 340.9 eV (Pd $3d_{3/2}$) (Fig. 2(c)) can be assigned to metallic $Pd^0$. The characteristic peaks at 71.0 and 74.3 eV in the Pt 4f spectrum (Fig. 2(d)) should be assigned to the binding energies of Pt $4f_{7/2}$ and Pt $4f_{5/2}$ of metallic $Pd^0$, respectively [31, 32]. Figures 3(a), 3(d), and 3(g) present typical TEM images of the as-synthesized M@MIL-100(Fe) nanocomposites. It can be observed that the integrity of the characteristic structure of MIL-100(Fe) is retained and not affected by the photodeposition processing, as confirmed by the above XRD analysis. The Au, Pd, and Pt NPs ingredients are homogeneously dispersed over MIL-100(Fe) with intimate interfacial contact (Figs. 3(b), 3(e), and 3(h)). The excellent dispersion of metal NPs on the MIL-100(Fe) can be attributed to the ultrahigh surface area and porosity of MIL-100(Fe), which can be expected on such highly dispersed metal NPs. The average diameters of the Au, Pd, and Pt NPs estimated

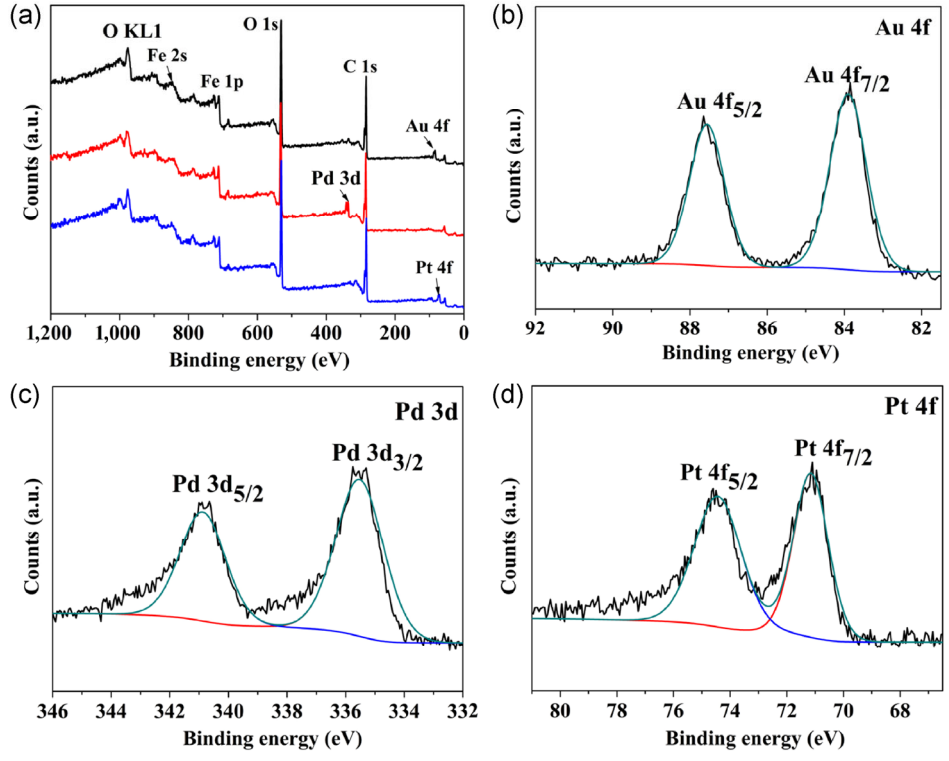


**Figure 2** XPS patterns of M@MIL-100(Fe) (M = Au, Pd, and Pt).

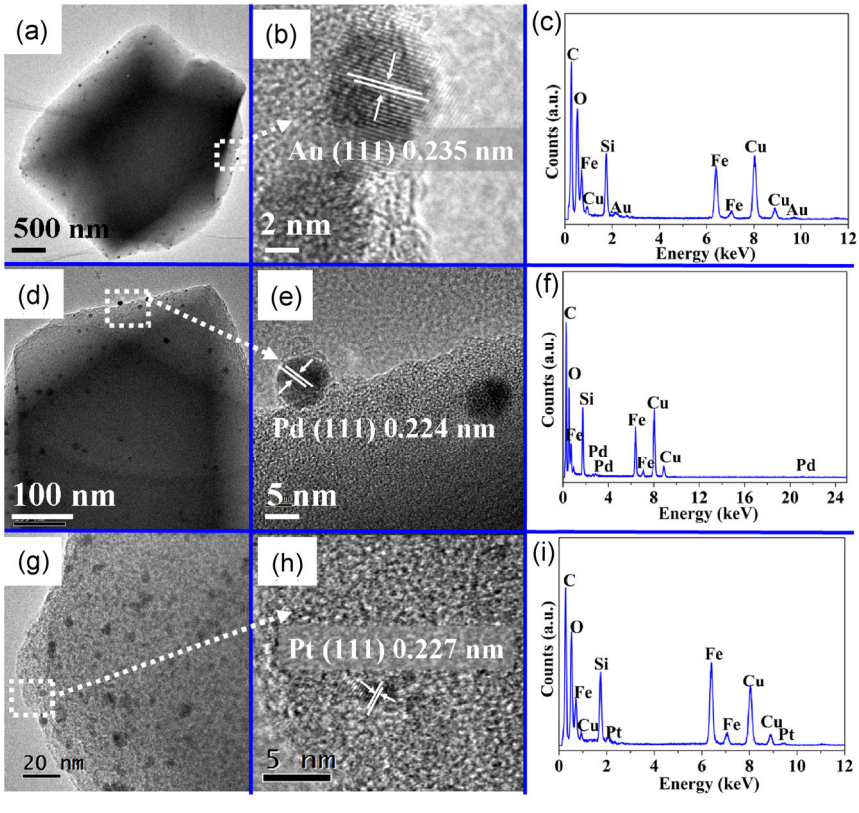


**Figure 3** TEM and HRTEM images of (a) and (b) Au@MIL-100(Fe), (d) and (e) Pd@MIL-100(Fe), and (g) and (h) Pt@MIL-100(Fe); EDX images of (c) Au@MIL-100(Fe), (f) Pd@MIL-100(Fe), and (i) Pt@MIL-100(Fe).

from Fig. S1 (in the Electronic Supplementary Material (ESM)) are 15, 12, and 2 nm, respectively. The HRTEM images in Figs. 3(b), 3(e), and 3(h) unambiguously show the characteristic lattice fringes of 0.235, 0.224, and 0.227 nm for Au, Pd, and Pt NPs, respectively, which can be indexed as the (111) planes of the noble metals [33–35]. To confirm the elemental composition of the M@MIL-100(Fe), energy-dispersive X-ray spectroscopy (EDX) was also performed. The results in Figs. 3(c), 3(f), and 3(i) reveal that the M@MIL-100(Fe) contain C, O, Fe, and Au/Pd/Pt, which is consistent with the XPS results. Using semiquantitative EDX analyses, the weight ratios of noble metal in the M@MIL-100(Fe) nanocomposites were roughly estimated to be 0.893, 0.937, and 1.027 wt% for Au@MIL-100(Fe), Pd@MIL-100(Fe), and Pt@MIL-100(Fe), respectively. In addition, the noble metal contents determined by ICP were approximately 0.818 wt.%, 0.930 wt.%, and 0.902 wt.% for Au@MIL-100(Fe), Pd@MIL-100(Fe), and Pt@MIL-100(Fe) nanocomposites, respectively (Table 1). There is a relative discrepancy between the EDX and ICP characterization results because of instrument errors. These results indicate that the facile photodeposition pathway is an effective technique to immobilize noble-metal NPs on MIL-100(Fe) because the noble metal content is very similar to the theoretical content (1 wt.%). The XPS, TEM, EDX, and ICP results confirm that the noble-metal (Au, Pd, and Pt) NPs on the MIL-100(Fe) surface exist predominantly in metallic form.

In addition, the surface area and pore structure of the samples were investigated, as displayed in Fig. 4. The nitrogen adsorption–desorption isotherms of the MIL-100(Fe) and M@MIL-100(Fe) (M = Au, Pd, and Pt) nanocomposites all exhibit type I isotherms according to the IUPAC classification, which are representative of microporous solids. To clearly see the variations of the original-MIL-100(Fe) after noble-metal deposition,

**Table 1** Weight ratios of noble metals in the M@MIL-100(Fe) (M = Au, Pd, and Pt) nanocomposites determined by ICP analysis

| Sample | Metal contents (wt.%) |
|---|---|
| Au@MIL-100(Fe) | 0.818 |
| Pd@MIL-100(Fe) | 0.930 |
| Pt@MIL-100(Fe) | 0.902 |

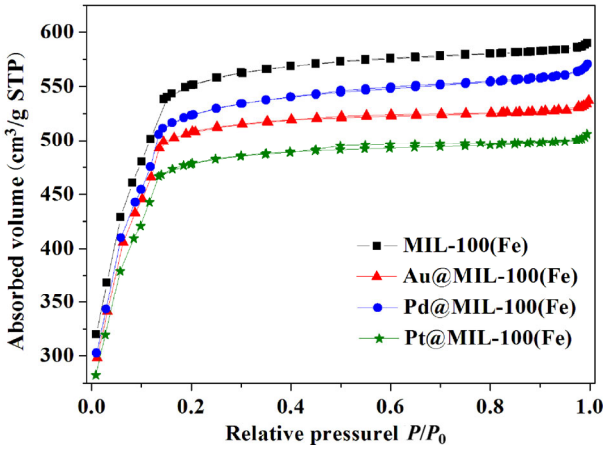


**Figure 4** BET adsorption–desorption isotherm of MIL-100(Fe) and M@MIL-100(Fe) (M = Au, Pd, and Pt).

we summarize the BET surface areas and pore volumes of the samples in Table S1 (in the ESM). The results indicate that both the BET surface areas and pore volumes of the M@MIL-100(Fe) decreased compared with those of the original-MIL-100(Fe). This result could be attributed to some of the MIL-100(Fe) pores being blocked by the loaded noble-metal NPs. As the photoabsorption property plays a key role in determining the photocatalytic activity, UV-vis DRS spectra of the samples were measured. Figure 5 presents the DRS spectra of MIL-100(Fe) and M@MIL-100(Fe) nanocomposites. For all the samples, an intense UV absorption band appears from 200 to 400 nm, which can be primarily attributed to absorption induced by ligand-to-metal charge transfer (LMCT) of O(II) → Fe(III) [36]. It can also be observed that the addition

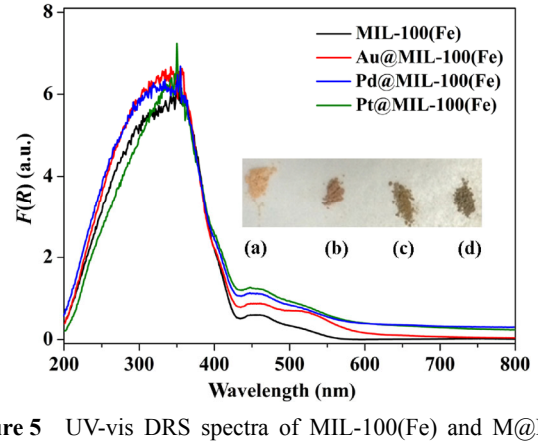


**Figure 5** UV-vis DRS spectra of MIL-100(Fe) and M@MIL-100(Fe) (M = Au, Pd, and Pt); photographs of (a) MIL-100(Fe), (b) Au@MIL-100(Fe), (c) Pd@MIL-100(Fe), and (d) Pt@MIL-100(Fe) are presented in the inset.

of the noble metal induces increased light absorption intensity in the visible region, which is in accordance with the color change of the M@MIL-100(Fe) samples (inset in Fig. 5). Thus, we can envision that the enhanced absorbance of light is expected to improve the photoactivity for a target reaction. This inference is well verified by the photocatalytic testing of MIL-100(Fe) and M@MIL-100(Fe) toward degradation of MO and reduction of Cr(VI) under visible light irradiation.

### 3.2 Photocatalytic properties

#### 3.2.1 *Photocatalytic degradation of aqueous MO*

The photocatalytic activities of MIL-100(Fe) and M@MIL-100(Fe) (M = Au, Pd, Pt) nanocomposites were evaluated by the photocatalytic degradation of aqueous MO under visible-light irradiation ($\lambda \geqslant 420$ nm). Figure S2 (in the ESM) shows the photocatalytic degradation of MO under various experimental conditions. It can be observed that the degradation of MO hardly occurs in the absence of light or a photocatalyst (curves a and b, respectively). After 150 min of visible-light irradiation, MIL-100(Fe) is able to degrade approximately 5% of MO (without $H_2O_2$, curve c), which may be attributed to a direct hole oxidation pathway. After injecting a certain amount of $H_2O_2$, MIL-100(Fe) becomes highly active (curve d). Moreover, the MIL-100(Fe) exhibits much higher activity than the N-doped $TiO_2$ or $Fe_2O_3$ (curves e and f, respectively) under identical experimental conditions. Figure 6(a) shows the photocatalytic activity for the degradation of MO under visible-light irradiation over the MIL-100(Fe) and M@MIL-100(Fe) (M = Au, Pd, Pt) nanocomposites. It is apparent that the decoration of the noble-metal NPs can effectively improve the photocatalytic performance of MIL-100(Fe) [37]. Among all of the samples, the Pt@MIL-100(Fe) nanocomposite exhibits the highest visible-light photoactivity toward the degradation of aqueous MO. After 40 min of visible-light irradiation, almost 100% MO can be degraded. Based on previous studies [11], the degradation of dyes can be attributed to a pseudo-first-order reaction with a simplified Langmuir–Hinshelwood model when $C_0$ is very small: $\ln(C_0/C_t) = kt$, where $k$ is the apparent first-order rate constant. As displayed in Fig. 6(b), the Pt@MIL-100(Fe) nanocomposite has the highest rate constant (0.07584 $min^{-1}$) among all of the samples. The kinetic rate constants follow the order Pt@MIL-100(Fe) > Pd@MIL-100(Fe) > Au@MIL-100(Fe) > MIL-100(Fe) (Table S2 in the ESM).

In addition, the stability and reusability of the samples were also investigated. After each cycling experiment, the photocatalyst was separated from the aqueous suspension by filtration and then washed with 1 M $HNO_3$ aqueous solution and deionized water several times to completely remove the absorbed MO on the surface of sample. Then, the photocatalyst was centrifuged and blow-dried with $N_2$. As observed in Fig. 7(a), the photocatalytic activities of MIL-100(Fe) and M@MIL-100(Fe) (M = Au, Pd, Pt) do not obviously decrease after four cycles, suggesting that the M@MIL-100(Fe) nanocomposites exhibit high stability in this reaction system. Moreover, XRD patterns (Fig. 7(b)) of the fresh and used samples reveal an intact crystalline

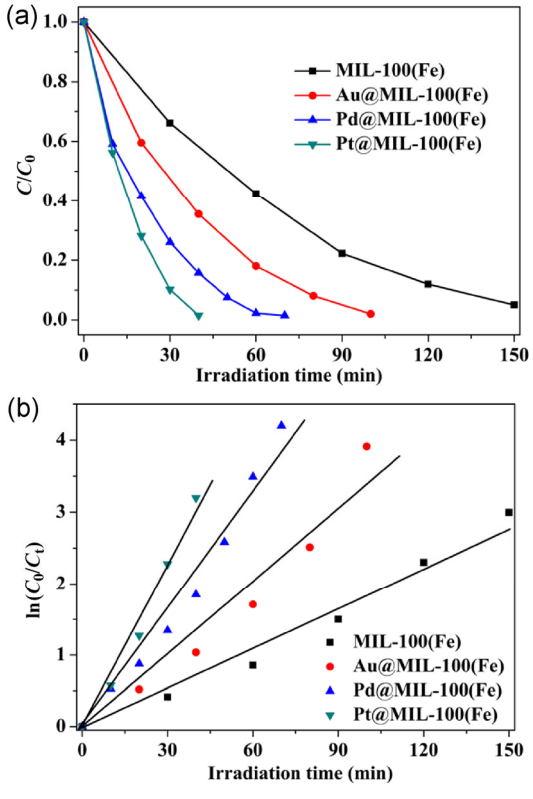


**Figure 6** (a) Photocatalytic degradation of MO over the MIL-100(Fe) and M@MIL-100(Fe) (M = Au, Pd, and Pt) under visible-light irradiation ($\lambda \geqslant 420$ nm); (b) kinetics of MO photocatalytic degradation over the MIL-100(Fe) and M@MIL-100(Fe) (M = Au, Pd, and Pt) (Reaction conditions: 5 mg photocatalyst, 40 mL of 20 ppm MO, 40 μL of $H_2O_2$, pH 4).

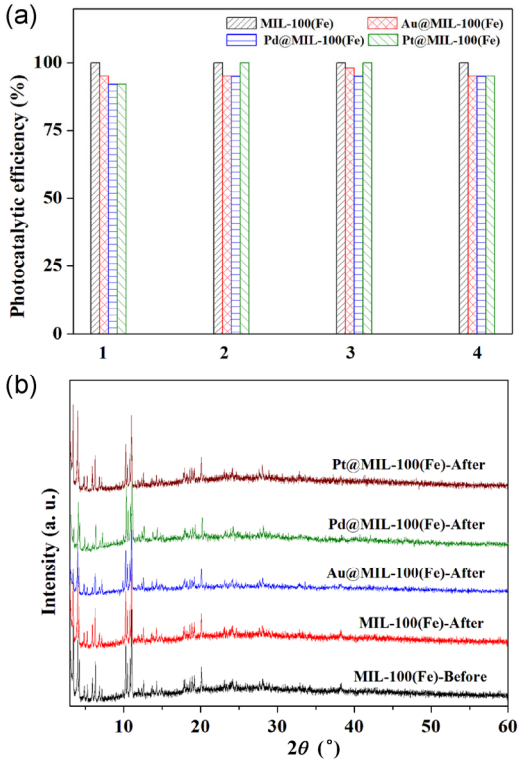


**Figure 7** (a) The reusability of MIL-100(Fe) and M@MIL-100(Fe) (M = Au, Pd, and Pt) for the photocatalytic degradation of MO; (b) XRD patterns of MIL-100(Fe) and M@MIL-100(Fe) (M = Au, Pd, and Pt) before and after the catalytic reaction.

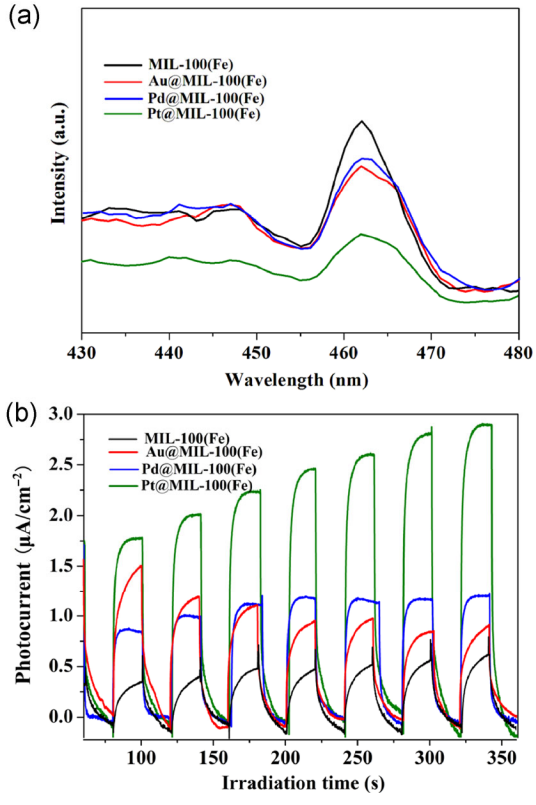


**Figure 8** (a) Transient photocurrent response of MIL-100(Fe) and M@MIL-100(Fe) (M = Au, Pd, and Pt) in 0.2 M $Na_2SO_4$ aqueous solution (pH 6.8) under visible-light irradiation ($\lambda \geqslant 420$ nm); (b) PL spectra of MIL-100(Fe) and M@MIL-100(Fe) (M = Au, Pd, and Pt) with an excitation wavelength of 340 nm.

structure of the M@MIL-100(Fe) after cycling experiments. As observed in the TEM images in Fig. S3 (in the ESM), no obvious morphology change of M@MIL-100(Fe) is observed after photocatalytic reactions, indicating that the characteristic structure of M@MIL-100(Fe) is retained. Additionally, the concentration of Fe(III) ions leaching during the reaction was quantified using an ICP optical emission spectrometer (Table S3, in the ESM). Apparently, almost no Fe(III) ions leach from the M@MIL-100(Fe) during the reaction. Furthermore, to determine the mineralization extent of MO, the TOC values of the MO aqueous solutions were also determined. Obviously, during the reaction, almost all of the MO can be mineralized (Table S4 in the ESM), which is consistent with the photocatalytic activity results.

To understand the origin of the remarkably different photoactivities of M@MIL-100(Fe) (M = Au, Pd, Pt), we performed photoelectrochemical experiments. Figure 8(a) displays the photocurrent transient response of MIL-100(Fe) and M@MIL-100(Fe) under intermittent visible-light illumination ($\lambda \geqslant 420$ nm). Pt@MIL-100(Fe) clearly exhibits the highest photocurrent density compared with the other samples, indicating a most efficient separation of the photogenerated electron–hole pairs, which can be further proved by the PL results. As displayed in Fig. 8(b), under an excitation wavelength of 340 nm, for MIL-100(Fe), a strong band at 450–480 nm with a peak at 464 nm is detected, which is attributed to the $H_3BTC$ linkers in the MIL-100(Fe) structure [38]. In addition, it can be observed that the intensity of the PL emission follows the order: MIL-100(Fe) > Au@MIL-100(Fe) > Pd@MIL-100(Fe) > Pt@MIL-100(Fe). A lower PL intensity is generally indicative of a lower recombination rate of photogenerated charge carriers [39–41]. Thus, we can conclude that the charge-separation efficiency follows the order: Pt@MIL-100(Fe) > Pd@MIL-100(Fe) > Au@MIL-100(Fe) > MIL-100(Fe), which is consistent with the MO degradation experiment results. In addition, considering that in M@MIL-100(Fe)

systems, the photoactive MIL-100(Fe) not only serves as a host to control the growth of metal NPs but also facilitates the separation of photogenerated charge carriers when the two components have intimate interfacial contact. Notably, the surface areas of MIL-100(Fe), Pd@MIL-100(Fe), Au@MIL-100(Fe), and Pt@MIL-100(Fe) were determined to be 2,007, 1,822, 1,989, and 1,724 $m^2/g$, respectively (Table S1 in the ESM). For all of these samples, the surface areas are quite similar to each other. Therefore, it appears that the observed photoactivity order, that is, Pt@MIL-100(Fe) > Pd@MIL-100(Fe) > Au@MIL-100(Fe) > MIL-100(Fe), cannot be attributed to the differences in surface area.

Accordingly, the higher photoactivity of M@MIL-100(Fe) can be attributed to the enhanced visible-light absorption, efficient charge-carrier separation, and synergistic effect between MIL-100(Fe) and metal NPs.

To better understand the intrinsic electronic properties of M@MIL-100(Fe), Mott-Schottky measurements were performed in darkness. As observed in Fig. S4 (in the ESM), the flat-band potential ($V_{fb}$) of the M@MIL-100(Fe) is approximately −0.60 V vs. Ag/AgCl at pH 6.8, corresponding to a potential of −0.40 V vs. NHE at pH 6.8. Combined with the band gap energy estimated from the UV-vis DRS spectrum, the VB of M@MIL-100(Fe) is calculated to be 2.41 V vs. NHE, according to the empirical formula $E_{CB} = E_{VB} - E_g$. The redox potential of MO is approximately 1.48 V vs. NHE [42], which is more negative than the VB value of M@MIL-100(Fe), suggesting that a direct hole oxidation pathway is available. As widely accepted, hydroxyl radicals (•OH) are the key active species in the $H_2O_2$-containing catalytic system, which have strong oxidative ability to attack most stable organic molecules. The formation of •OH in the catalytic systems of M@MIL-100(Fe)/MO/$H_2O_2$ was detected by active species trapping experiments. As demonstrated in Fig. S5 (in the ESM), the addition of tert-butyl alcohol (TBA, a •OH scavenger) could induce the depression effect on the photocatalytic degradation of MO. Clearly, approximately 40.2%, 29.1%, 35.8%, and 37.0% inhibition are observed in the MIL-100(Fe), Au@MIL-100(Fe), Pd@MIL-100(Fe), and Pt@MIL-100(Fe) systems, respectively. The inhibitory effect of TBA indicates that the •OH in the reaction system plays an important role for photocatalytic degradation of MO.

Based on the above results, a reaction mechanism for photocatalytic degradation of MO over M@MIL-100(Fe) (M = Au, Pd, Pt) nanocomposites is proposed (Fig. 9). Under visible-light irradiation ($\lambda \geqslant 420$ nm), M@MIL-100(Fe) nanocomposites are excited and electron–hole pairs are generated. Subsequently, the decorated noble-metal particles can accept the photogenerated electrons and prolong the lifetime of charge carriers. The porous structure of MOFs can also provide extra pathways for the migration of photoinduced electrons and thus facilitate the charge-carrier separation. Moreover, the ultrahigh surface area of MIL-100(Fe) enables better contact between reactants and active sites, which may create more catalytic sites. The $H_2O_2$ reacts with the photogenerated electrons to form •OH. In addition, the photogenerated holes, which generally contribute to the oxidation reaction, can directly oxidize the adsorbed MO. More significantly, the Fe(III)-O clusters on the surface of M@MIL-100(Fe) can catalyze the decomposition of $H_2O_2$ to produce more •OH radicals exhibiting a strong oxidation capacity to oxidize the surface-adsorbed organic molecules (Eqs. (1) and (2)). Accordingly, the above processes could cooperatively contribute to produce more photogenerated holes and •OH radicals, thus greatly enhancing the degradation efficiency of MO.

$$\text{Fe(III) species} + H_2O_2 \rightarrow \text{Fe(II) species} + \bullet HOO + H^+ \quad (1)$$

$$\text{Fe(II) species} + H_2O_2 \rightarrow \text{Fe(III) species} + \bullet OH + OH^- \quad (2)$$

### 3.2.2 Photocatalytic reduction of Cr(VI)

The more efficient enhancement of the rate and transfer

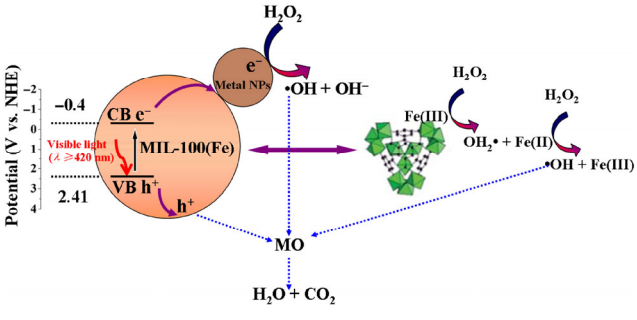


**Figure 9** Schematic diagram of the proposed mechanism for MO photocatalytic degradation over the M@MIL-100(Fe) (M = Au, Pd, and Pt) under visible-light irradiation ($\lambda \geqslant 420$ nm).

of photogenerated charge carriers in M@MIL-100(Fe) (M = Au, Pd, Pt) compared with those in MIL-100(Fe) can also be verified by the photocatalytic reduction of Cr(VI) to Cr(III) under visible-light irradiation. This reduction is an important environmental remediation step because of the increasing use of Cr(VI) compounds in various industries, such as metal plating and tanneries [43, 44]. Blank experiments were first performed to demonstrate the photocatalytic nature of the reaction (Fig. S6 in the ESM). Considering the overall activities from Fig. 10, it can be observed that similar to the case of the photocatalytic degradation of MO, as discussed above, the deposition of noble metals can effectively promote the photocatalytic reduction process of the original-MIL-100(Fe). Pt@MIL-100(Fe) can completely reduce the Cr(VI) within 8 min, whereas only 69% of Cr(VI) is reduced over MIL-100(Fe). To better understand the photocatalysis process of M@MIL-100(Fe) (M = Au, Pd, Pt), we further compared the kinetic rate constants obtained from the above experimental processes. As summarized in Table S5 (in the ESM), the kinetic rate constants for the photocatalytic reduction of Cr(VI) follow the order Pt@MIL-100(Fe) (0.5618 $min^{-1}$) > Pd@MIL-100(Fe) (0.2883 $min^{-1}$) > Au@MIL-100(Fe) (0.1861 $min^{-1}$) > MIL-100(Fe) (0.1518 $min^{-1}$). This result is also in good agreement with the charge-carrier separation efficiency, as verified by the PL analysis. Thus, it can be concluded that the Pt NPs with smaller particle size are much more favorable for the enhancement of MIL-100(Fe) photoactivity for both photocatalytic degradation of MO and reduction of Cr(VI) than the noble-metal (Au and Pt) NPs with larger particle size. This result most likely occurs because the smaller particle size of the noble metal is generally more favorable for charge-carrier separation of photogenerated electron–hole pairs, which can be inferred from the controlled experiments. Taking the Pt@MIL-100(Fe) system as an example, as displayed in Figs. S7 and S8 (in the ESM), further increasing the photodeposition time leads to a photocatalytic activity deterioration of the Pt@MIL-100(Fe) nanocomposites. This deterioration mainly occurs because the Pt NPs grow and aggregate on the surface of the MOFs, resulting in reduced interfacial contact between the Pt NPs and MIL-100(Fe). For the activity stability, the photocatalytic activities of M@MIL-100(Fe) do not obviously decrease in any of the recycling experiments (Fig. 11 and Table S6 in the ESM). Trapping experiments using $AgNO_3$ as an electron scavenger

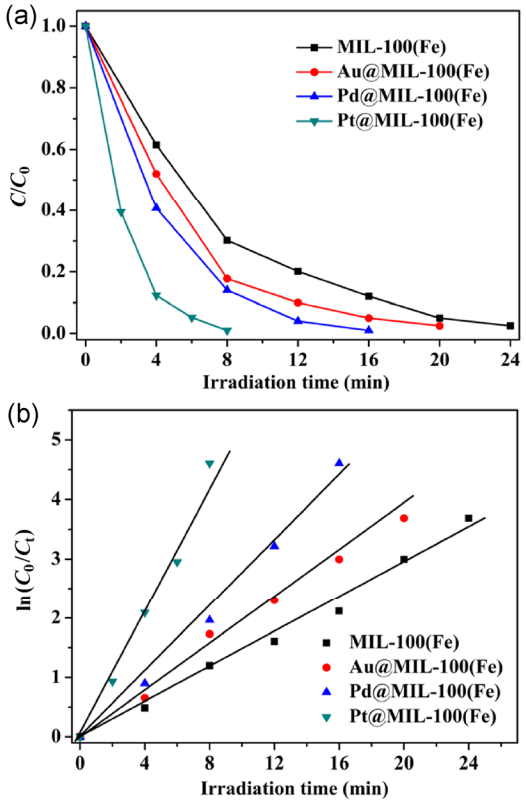


**Figure 10** (a) Photocatalytic reduction of Cr(VI) over the MIL-100(Fe) and M@MIL-100(Fe) (M = Au, Pd, and Pt) under visible-light irradiation ($\lambda \geqslant 420$ nm); (b) kinetics of Cr(VI) reduction over the MIL-100(Fe) and M@MIL-100(Fe) (M = Au, Pd, and Pt) (Reaction conditions: 40 mg photocatalyst, 40 mL of 20 ppm Cr(VI), 5 mg of ammonium oxalate, pH 4).

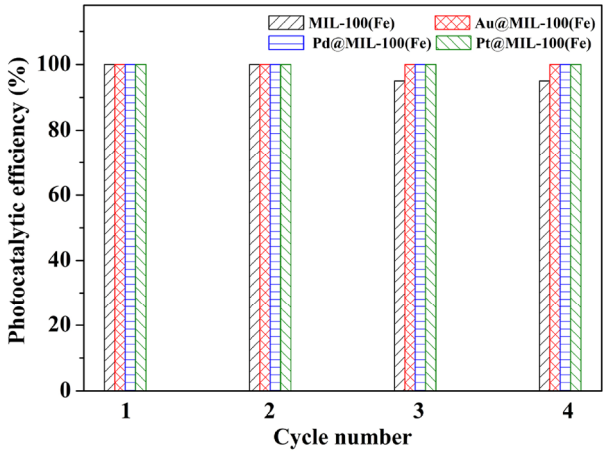


**Figure 11** The reusability of the MIL-100(Fe) and M@MIL-100(Fe) (M = Au, Pd, and Pt) for the photocatalytic reduction of Cr(VI).

for photogenerated electrons confirmed that the photoreduction of Cr(VI) is driven by photogenerated electrons (Fig. S9 in the ESM).

Accordingly, a probable mechanism for the reduction of Cr(VI) over M@MIL-100(Fe) (M = Au, Pd, Pt) has been proposed (Fig. 12). Under visible-light irradiation, the photogenerated charge carriers migrate to the surface of the MIL-100(Fe) and participate in the redox reaction. The photogenerated holes are trapped by the ammonium oxalate. Simultaneously, the photogenerated electrons can reduce Cr(VI) to Cr(III). Because of the synergetic effect between MIL-100(Fe) and the noble-metal NPs, the photogenerated charge carriers can be more efficiently separated, thereby enhancing the photoactivity.

## 4 Conclusions

In summary, a series of novel M@MIL-100(Fe) (M = Au, Pd, Pt) nanocomposites were successfully fabricated via a facile photochemical route. The resulting M@MIL-100(Fe) nanocomposites were effective not only toward photocatalytic degradation of MO but also for the reduction of Cr(VI) in water under visible-light irradiation ($\lambda \geqslant 420$ nm). In contrast to MIL-100(Fe), the M@MIL-100(Fe) nanocomposites exhibited enhanced photocatalytic performance for both the oxidation and reduction processes. The enhanced photoactivity relies crucially on the contribution of noble-metal particles acting as electron reservoirs in prolonging the lifetime of photogenerated charge carriers. In particular, the Pt@MIL-100(Fe) with an average Pt particle size of 2 nm exhibited remarkably enhanced photoactivities compared with those of M@MIL-100(Fe) (M = Au and Pd), which can be attributed to the integrative effect of the enhanced light absorption intensity and more efficient separation of the photogenerated charge carriers. Our current work could not only widen the application range of MOFs but also provide useful information for synthesizing high-performance M@MOFs for restoration of the environment.

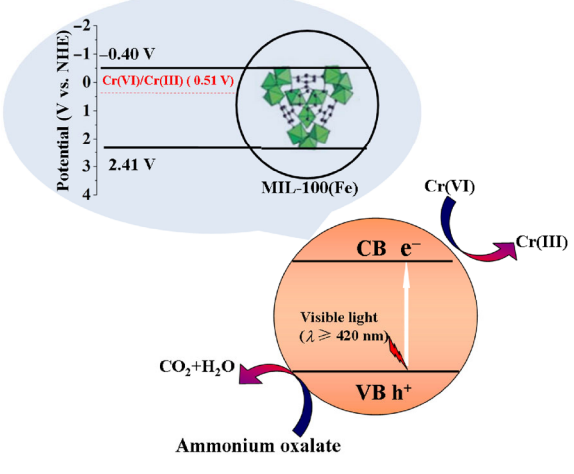


**Figure 12** A schematic illustration of the photocatalytic reduction of Cr(VI) over M@MIL-100(Fe) (M = Au, Pd, and Pt) under visible-light irradiation ($\lambda \geqslant 420$ nm).

## Acknowledgements

This work was supported by the National Natural Science Foundation of China (Nos. 21273036 and 21177024) and Science & Technology Plan Project of Fujian Province (No. 2014Y2003).

**Electronic Supplementary Material**: Supplementary material (size distribution plots of Au, Pd, Pt NPs; the surface area and pore volume of samples; TEM images; control experiment results; blank experiment results; trapping experiment results; the pseudo-first order rate constants; typical Mott-Schottky plots; the effect of particle size on photoactivities; the concentration of Fe(III) during the reaction; the TOC values during the reaction) is available in the online version of this article at http://dx.doi.org/10.1007/s12274-015-0824-9.

## References

[1] Ferey, G. Hybrid porous solids: Past, present, future. *Chem. Soc. Rev.* **2008**, *37*, 191–214.

[2] Horiuchi, Y.; Toyao, T.; Saito, M.; Mochizuki, K.; Iwata, M.; Higashimura, H.; Anpo, M.; Matsuoka, M. Visible-light-promoted photocatalytic hydrogen production by using an amino-functionalized Ti(IV) metal-organic framework. *J. Phys. Chem. C* **2012**, *116*, 20848–20853.

[3] Kitagawa, S.; Kitaura, R.; Noro, S. Functional porous coordination polymers. *Angew. Chem., Int. Ed.* **2004**, *43*, 2334–2375.

[4] Vallet-Regi, M.; Balas, F.; Arcos, D. Mesoporous materials for drug delivery. *Angew. Chem., Int. Ed.* **2007**, *46*, 7548–7558.

[5] Lee, J.; Farha, O. K.; Roberts, J.; Scheidt, K. A.; Nguyen, S. T.; Hupp, J. T. Metal-organic framework materials as catalysts. *Chem. Soc. Rev.* **2009**, *38*, 1450–1459.

[6] Millward, A. R.; Yaghi, O. M. Metal-organic frameworks with exceptionally high capacity for storage of carbon dioxide at room temperature. *J. Am. Chem. Soc.* **2005**, *127*, 17998–17999.

[7] Harbuzaru, B. V.; Corma, A.; Rey, F.; Atienzar, P.; Jorda, J. L.; Garcia, H.; Ananias, D.; Carlos, L. D.; Rocha, J. Metal-organic nanoporous structures with anisotropic photo-luminescence and magnetic properties and their use as sensors. *Angew. Chem., Int. Ed.* **2008**, *47*, 1080–1083.

[8] Janiak, C. Engineering coordination polymers towards applications. *Dalton Trans.* **2003**, 2781–2804.

[9] Zhou, L. M.; Zhang, T. R.; Tao, Z. L.; Chen, J. Ni nano-particles supported on carbon as efficient catalysts for the hydrolysis of ammonia borane. *Nano Res.* **2014**, *7*, 774–781.

[10] Ke, F.; Wang, L. H.; Zhu, J. F. Facile fabrication of CdS metal-organic framework nanocomposites with enhanced visible-light photocatalytic activity for organic transformation. *Nano Res.* **2015**, *8*, 1834–1846.

[11] Liang, R. W.; Jing, F. F.; Shen, L. J.; Qin, N.; Wu, L. MIL-53(Fe) as a highly efficient bifunctional photocatalyst for the simultaneous reduction of Cr(VI) and oxidation of dyes. *J. Hazard. Mater.* **2015**, *287*, 364–372.

[12] Liang, R. W.; Shen, L. J.; Jing, F. F.; Wu, W. M.; Qin, N.; Lin, R.; Wu, L. $NH_2$-mediated indium metal-organic framework as a novel visible-light-driven photocatalyst for reduction of the aqueous Cr(VI). *Appl. Catal. B: Environ.* **2015**, *162*, 245–251.

[13] Shen, L. J.; Liang, S. J.; Wu, W. M.; Liang, R. W.; Wu, L. Multifunctional $NH_2$-mediated zirconium metal-organic framework as an efficient visible-light-driven photocatalyst for selective oxidation of alcohols and reduction of aqueous Cr(VI). *Dalton Trans.* **2013**, *42*, 13649–13657.

[14] Zhang, C.-F.; Qiu, L.-G.; Ke, F.; Zhu, Y.-J.; Yuan, Y.-P.; Xu, G.-S.; Jiang, X. A novel magnetic recyclable photocatalyst based on a core-shell metal-organic framework $Fe_3O_4$@MIL-100(Fe) for the decolorization of methylene blue dye. *J. Mater. Chem. A* **2013**, *1*, 14329–14334.

[15] Liu, N. A.; Yao, Y.; Cha, J. J.; McDowell, M. T.; Han, Y.; Cui, Y. Functionalization of silicon nanowire surfaces with metal-organic frameworks. *Nano Res.* **2012**, *5*, 109–116.

[16] Wu, M.-C.; Sápi, A.; Avila, A.; Szabó, M.; Hiltunen, J.; Huuhtanen, M.; Tóth, G.; Kukovecz, Á.; Kónya, Z.; Keiski, R. et al. Enhanced photocatalytic activity of $TiO_2$ nanofibers and their flexible composite films: Decomposition of organic dyes and efficient $H_2$ generation from ethanol-water mixtures. *Nano Res.* **2011**, *4*, 360–369.

[17] Zhou, W.; Li, T.; Wang, J. Q.; Qu, Y.; Pan, K.; Xie, Y.; Tian, G. H.; Wang, L.; Ren, Z. Y.; Jiang, B. J. et al. Composites of small Ag clusters confined in the channels of well-ordered mesoporous anatase $TiO_2$ and their excellent solar-light-driven photocatalytic performance. *Nano Res.* **2014**, *7*, 731–742.

[18] Hua, Q.; Shi, F. C.; Chen, K.; Chang, S. J.; Ma, Y. S.; Jiang, Z. Q.; Pan, G. Q.; Huang, W. X. $Cu_2O$-Au nanocomposites with novel structures and remarkable chemisorption capacity and photocatalytic activity. *Nano Res.* **2011**, *4*, 948–962.

[19] Zhou, X. M.; Liu, G.; Yu, J. G.; Fan, W. H. Surface plasmon resonance-mediated photocatalysis by noble-metal-based composites under visible light. *J. Mater. Chem.* **2012**, *22*, 21337–21354.

[20] Tada, H.; Kiyonaga, T.; Naya, S. Rational design and applications of highly efficient reaction systems photocatalyzed by noble-metal nanoparticle-loaded titanium(IV) dioxide. *Chem. Soc. Rev.* **2009**, *38*, 1849–1858.

[21] Shen, L. J.; Wu, W. M.; Liang, R. W.; Lin, R.; Wu, L. Highly dispersed palladium nanoparticles anchored on UiO-66($NH_2$) metal-organic framework as a reusable and dual functional visible-light-driven photocatalyst. *Nanoscale* **2013**, *5*, 9374–9382.

[22] Meilikhov, M.; Yusenko, K.; Esken, D.; Turner, S.; Van Tendeloo, G.; Fischer, R. A. Metals@MOFs loading MOFs with metal nanoparticles for hybrid functions. *Eur. J. Inorg. Chem.* **2010**, *2010*, 3701–3714.

[23] Hou, C.; Zhao, G. F.; Ji, Y. J.; Niu, Z. Q.; Wang, D. S.; Li, Y. D. Hydroformylation of alkenes over rhodium supported on the metal-organic framework ZIF-8. *Nano Res.* **2014**, *7*, 1364–1369.

[24] Jiang, H.-L.; Liu, B.; Akita, T.; Haruta, M.; Sakurai, H.; Xu, Q. Au@ZIF-8: CO oxidation over gold nanoparticles deposited to metal-organic framework. *J. Am. Chem. Soc.* **2009**, *131*, 11302–11303.

[25] Cheon, Y. E.; Suh, M. P. Enhanced hydrogen storage by palladium nanoparticles fabricated in a redox-active metal-organic framework. *Angew. Chem., Int. Ed.* **2009**, *48*, 2899–2903.

[26] El-Shall, M. S.; Abdelsayed, V.; Khder, A. E. R. S.; Hassan, H. M. A.; El-Kaderi, H. M.; Reich, T. E. Metallic and bimetallic nanocatalysts incorporated into highly porous coordination polymer MIL-101. *J. Mater. Chem.* **2009**, *19*, 7625–7631.

[27] Horcajada, P.; Surble, S.; Serre, C.; Hong, D.-Y.; Seo, Y.-K.; Chang, J.-S.; Greneche, J.-M.; Margiolaki, I.; Ferey, G. Synthesis and catalytic properties of MIL-100(Fe), an iron(Ⅲ) carboxylate with large pores. *Chem. Commun.* **2007**, 2820–2822.

[28] Idris, A.; Hassan, N.; Rashid, R.; Ngomsik, A.-F. Kinetic and regeneration studies of photocatalytic magnetic separable beads for chromium (VI) reduction under sunlight. *J. Hazard. Mater.* **2011**, *186*, 629–635.

[29] Pan, X. Y.; Xu, Y.-J. Fast and spontaneous reduction of gold ions over oxygen-vacancy-rich $TiO_2$: A novel strategy to design defect-based composite photocatalyst. *Appl. Catal. A: Gen.* **2013**, *459*, 34–40.

[30] Liu, X.; Ye, S.; Li, H.-Q.; Liu, Y.-M.; Cao, Y.; Fan, K.-N. Mild, selective and switchable transfer reduction of nitroarenes catalyzed by supported gold nanoparticles. *Catal. Sci. Technol.* **2013**, *3*, 3200–3206.

[31] Gu, X. J.; Lu, Z.-H.; Jiang, H.-L.; Akita, T.; Xu, Q. Synergistic catalysis of metal-organic framework-immobilized Au-Pd nanoparticles in dehydrogenation of formic acid for chemical hydrogen storage. *J. Am. Chem. Soc.* **2011**, *133*, 11822–11825.

[32] Chen, S. F.; Li, J. P.; Qian, K.; Xu, W. P.; Lu, Y.; Huang, W. X.; Yu, S. H. Large scale photochemical synthesis of M@$TiO_2$ nanocomposites (M = Ag, Pd, Au, Pt) and their optical properties, CO oxidation performance, and antibacterial effect. *Nano Res.* **2010**, *3*, 244–255.

[33] Zheng, Z. K.; Huang, B. B.; Qin, X. Y.; Zhang, X. Y.; Dai, Y.; Whangbo, M.-H. Facile *in situ* synthesis of visible-light plasmonic photocatalysts M@$TiO_2$ (M = Au, Pt, Ag) and evaluation of their photocatalytic oxidation of benzene to phenol. *J. Mater. Chem.* **2011**, *21*, 9079–9087.

[34] Teranishi, T.; Miyake, M. Size control of palladium nanoparticles and their crystal structures. *Chem. Mater.* **1998**, *10*, 594–600.

[35] Zhang, N.; Liu, S. Q.; Fu, X. Z.; Xu, Y.-J. Synthesis of M@$TiO_2$ (M = Au, Pd, Pt) core-shell nanocomposites with tunable photoreactivity. *J. Phys. Chem. C* **2011**, *115*, 9136–9145.

[36] Bordiga, S.; Lamberti, C.; Ricchiardi, G.; Regli, L.; Bonino, F.; Damin, A.; Lillerud, K. P.; Bjorgen, M.; Zecchina, A. Electronic and vibrational properties of a MOF-5 metal-organic framework: ZnO quantum dot behaviour. *Chem. Commun.* **2004**, 2300–2301.

[37] Pan, X. Y.; Xu, Y.-J. Defect-mediated growth of noble-metal (Ag, Pt, and Pd) nanoparticles on $TiO_2$ with oxygen vacancies for photocatalytic redox reactions under visible light. *J. Phys. Chem. C* **2013**, *117*, 17996–18005.

[38] Allendorf, M. D.; Bauer, C. A.; Bhakta, R. K.; Houk, R. J. T. Luminescent metal-organic frameworks. *Chem. Soc. Rev.* **2009**, *38*, 1330–1352.

[39] Liu, X. W.;Cao, H. Q.; Yin, J. F. Generation and photocatalytic activities of Bi@$Bi_2O_3$ microspheres. *Nano Res.* **2011**, *4*, 470–482.

[40] Gao, B.; Lin, Y.; Wei, S. J.; Zeng, J.; Liao, Y.; Chen, L. G.; Goldfeld, D.; Wang, X. P.; Luo, Y.; Dong, Z. C. et al. Charge transfer and retention in directly coupled Au-CdSe nanohybrids. *Nano Res.* **2012**, *5*, 88–98.

[41] Zhang, Y. H.; Zhang, N.; Tang, Z.-R.; Xu, Y.-J. Improving the photocatalytic performance of graphene-$TiO_2$ nanocomposites via a combined strategy of decreasing defects of graphene and increasing interfacial contact. *Phys. Chem. Chem. Phys.* **2012**, *14*, 9167–9175.

[42] Yan, S. C.; Li, Z. S.; Zou, Z. G. Photodegradation of rhodamine B and methyl orange over boron-doped g-$C_3N_4$ under visible light irradiation. *Langmuir* **2010**, *26*, 3894–3901.

[43] Wang, X. L.; Pehkonen, S. O.; Ray, A. K. Removal of aqueous Cr(VI) by a combination of photocatalytic reduction and coprecipitation. *Ind. Eng. Chem. Res.* **2004**, *43*, 1665–1672.

[44] Khalil, L. B.; Mourad, W. E.; Rophael, M. W. Photocatalytic reduction of environmental pollutant Cr(VI) over some semiconductors under UV/visible light illumination. *Appl. Catal. B: Environ.* **1998**, *17*, 267–273.

[45] Navío, J. A.; Colón, G.; Trillas, M.; Peral, J.; Domènech, X.; Testa, J. J.; Padrón, J.; Rodríguez, D.; Litter, M. I. Heterogeneous photocatalytic reactions of nitrite oxidation and Cr(VI) reduction on iron-doped titania prepared by the wet impregnation method. *Appl. Catal. B: Environ.* **1998**, *16*, 187–196.